Numerical Simulation Study on Aerodynamic Interference Characteristics of Overlapping Rotors in Heavy-Load eVTOL Aircraft

DU Siliang[1,2*], *DENG Kai*[2], *WANG Bo*[2]

1. Faculty of Mechanical & Material Engineering, Huai'an University, Huai'an 223003, P. R. China;
2. National Key Laboratory of Helicopter Aeromechanics, Nanjing University of Aeronautics and Astronautics, Nanjing 210016, P. R. China

(Received 21 September 2025; revised 18 November 2025; accepted 30 November 2025)

Abstract: Focusing on the unclear mechanism of aerodynamic interference in overlapping rotors of heavy-load electric vertical take-off and landing (eVTOL) aircraft, this paper aims to reveal the aerodynamic interference characteristics and flow field evolution laws of overlapping rotor configurations in hovering conditions through numerical simulation methods. The research method involves constructing a computational model for rotor flow fields and aerodynamic characteristics based on the Reynolds-averaged Navier-Stokes (RANS) equations and the Spalart-Allmaras (S-A) turbulence model. The dynamic simulation of rotor rotational motion was achieved by using the moving nested grid technology. The reliability of the computational method was ensured through the grid independence verification and the comparison with experimental data. The research results indicate that in overlapping rotor systems, rotor Ⅱ experiences a decrease in thrust, significant power fluctuations, and reduced hovering efficiency due to continuous interference from the adjacent rotor's wake and blade-vortex interactions. Blade-tip vortices undergo breakage, fusion, and secondary rolling in the overlapping region, forming large-scale turbulent structures that lead to attenuation of the induced velocity field and aerodynamic efficiency losses. Additionally, the interaction between the rotor downwash and the fuselage triggers a "fountain effect" and a sudden increase in surface pressure on the fuselage, exacerbating flow field distortion. Based on the aforementioned mechanisms, the safe flight of overlapping rotor configurations can be achieved by optimizing the configuration strategy of the rotational speed phase difference between adjacent blades. This study provides a theoretical basis for the rotor layout design and the aerodynamic performance enhancement of heavy-load eVTOL aircraft.

Key words: electric vertical takeoff and landing (eVTOL) aircraft; overlapping rotors; aerodynamic interference; numerical simulation; rotor vortex interference

CLC number: V211.7 **Document code:** A **Article ID:** 1005-1120(2026)01-0040-15

0 Introduction

In recent years, the continuous deterioration of urban traffic congestion and the gradual opening of low-altitude airspace management policies have created dual driving forces for technological innovation in electric vertical take-off and landing (eVTOL) aircraft. Against the backdrop of the integrated development of energy transformation and intelligent control technologies, heavy-load eVTOL aircraft (with a take-off weight exceeding 1 ton) are emerging as vital carriers for urban air mobility systems due to their large payload capacity, low carbon emissions, and adaptability to multi-dimensional transportation[1]. However, for practical engineering applications, heavy-load eVTOL aircraft still face significant technical bottlenecks in aerodynamic layout optimization and control response efficiency. Tradi-

*Corresponding author, E-mail address: kjofchina@qq.com.

How to cite this article: DU Siliang, DENG Kai, WANG Bo. Numerical simulation study on aerodynamic interference characteristics of overlapping rotors in heavy-load eVTOL aircraft[J]. Transactions of Nanjing University of Aeronautics and Astronautics, 2026, 43(1): 40-54.

http://dx.doi.org/10.16356/j.1005-1120.2026.01.004

tional helicopter rotor systems employ a single-rotor configuration, which consist of components such as swashplates and pitch-change hubs. The rotor rotation depends on a reduction gear mechanism to transmit engine power, leading to a complex overall structure. These complex structures represent dead weight for the aircraft, and if traditional helicopter rotor configurations are used to develop large-payload distributed VTOL aircraft, the transmission and pitch-change mechanisms would become extremely complex, not only increasing the aircraft's weight and volume but also significantly reducing system reliability.

With the development of eVTOL technology, it has become feasible to directly drive rotor rotation using high-power electric motors, enabling control of flight attitude through adjustments in the rotational speeds of distributed rotors. This approach effectively simplifies the aircraft structure, reduces weight, and improves reliability, representing a promising direction for future development. However, the coupling mechanisms of aerodynamic interference in multi-rotor systems remain unclear, limiting the overall performance of the aircraft.

In the field of aerodynamic interference research, scholars both domestically and abroad have conducted systematic studies on the aerodynamic characteristics of different rotor configurations. Early foreign research focused on the mechanism exploration of coaxial twin rotors. For instance, Syal et al.[2] revealed the wake interference patterns of coaxial rotors in hover through aerodynamic optimization, providing a theoretical basis for rotor spacing design. Hayami et al.[3] employed numerical simulation methods to quantify pressure fluctuation characteristics in the unsteady flow field of coaxial rotors, elucidating the causes of aerodynamic load distortion. In addition to conventional aerodynamic interference analyses of coaxial twin rotors and helicopter rotor-fuselage interactions[4-6], as well as layout structural parameter optimization and experiments[7-8], domestic research has further extended to the aerodynamic interference analysis of complex configurations. Refs.[9-10] summarized the aerodynamic interference characteristics between rotors of coaxial compound high-speed helicopters and methods for aerodynamic structure optimization. Zhu et al.[11] revealed the vortex coupling mechanism of coaxial rigid twin rotors through unsteady flow simulations, identifying wake impact as a key factor in induced vibration amplification. Cui et al.[12] constructed a high-precision prediction model for the vertical flight performance of high-speed helicopters based on the computational fluid dynamics (CFD) method, providing a tool for dynamic interference analysis. Refs.[13-14] conducted extensive research on the aerodynamic interference between tandem helicopter rotors, and analyzed the effects of non-twisted and twisted blades on aerodynamic interference through wind tunnel tests and numerical simulations. They found that wake interactions between rotors lead to changes in rotor lift coefficient and power coefficient, thereby affecting flight performance. In recent years, distributed ducted fans and compound tilt-rotor configurations have become research hotspots. Li et al.[15] discovered that the local increase in the turbulent kinetic energy of ducted multi-rotors could reach 40% and proposed an active flow control strategy. Wang et al.[16] revealed the evolution patterns of rotor-fuselage interference flow fields in hover for a dual-thrust compound configuration. Refs.[17-18] conducted a parametric analysis of the aerodynamic interference characteristics of tilt-rotor unmanned aerial vehicles during transition states.

Although the aforementioned achievements have laid an important foundation for rotor aerodynamic interference research, existing studies have primarily focused on conventional configurations, such as traditional quadrotors and coaxial twin rotors. There are still significant gaps in the exploration of aerodynamic interference in overlapping rotors of heavy-load eVTOL aircraft. Despite becoming an important development direction for urban air mobility because of their spatial compactness and layout flexibility, the aerodynamic design of this configuration faces multiple challenges. First, there is a contradiction in the collaborative optimization of rotor quantity and spatial layout. Increasing redundancy for safety exacerbates three-dimensional vortex interference effects, leading to lift loss and a substantial increase in system weight. Second, the unsteady dynamic interference between rotors and the fuselage induced by compact layouts remains unclear.

High-frequency pressure fluctuations potentially induce structural resonance and threatening flight stability. Third, the coupling constraints between the high inertia characteristics of large-sized rotors and the response lag of the power system make it difficult for traditional drive technologies to meet precise control requirements under heavy-load conditions. Therefore, there is an urgent need to conduct in-depth exploration of the aerodynamic interference mechanisms and optimization methods for overlapping rotor configurations to overcome the key technical bottlenecks of heavy-load eVTOL aircraft. With the accelerated implementation of eVTOL technology in urban low-altitude transportation, new concept vehicles, such as the Xpeng Aeroht "Land Aircraft Carrier" modular flying car, are driving the industry toward large-scale applications. This model features an innovative overlapping rotor layout design, has completed engineering prototype manufacturing, and has entered the airworthiness certification phase. Its maximum take-off mass of 880 kg marks a breakthrough in large-scale eVTOL technology. However, significant gaps remain in academic and industrial research on the aerodynamic characteristics of overlapping rotor configurations. Existing research has primarily focused on the aerodynamic interference analysis of small and medium-sized unmanned aerial vehicles. There is a lack of systematic theoretical support for key issues such as multi-rotor coupling effects, dynamic interference suppression, and aerodynamic efficiency optimization in large-scale platforms with take-off mass exceeding 150 kg, particularly in complex urban low-altitude scenarios. This lag in technical understanding compared to engineering practice not only restricts the aerodynamic design optimization of heavy-load eVTOL vehicles but may also pose safety risks for their future large-scale deployment in urban air mobility.

In light of this, this paper focuses on large-scale overlapping rotor eVTOL systems. It reveals the evolution patterns of aerodynamic interference in overlapping rotor layouts through numerical simulations and dynamic interference feature extraction, and provides theoretical support for the engineering design and airworthiness certification of heavy-load eVTOL aircraft.

1 Computational Model and Numerical Method

1.1 eVTOL aircraft and rotor model

The heavy-load eVTOL aircraft designed in this study has a standard take-off mass of 2.7 t and a maximum take-off mass of 4 t. The rotor layout adopts an H6 overlapping configuration (Fig.1), with a designed rotor diameter of 3.2 m and a blade tip speed of 216.7 m/s. Under the standard take-off mass, the hovering thrust of a single rotor without ground effect should exceed 450 kg, with a required power not exceeding 90 kW.

Fig.1 Heavy-load eVTOL aircraft

Fig.2 illustrates the airfoil configuration, chord length, and negative twist distribution along the blade span (r/R) of the rotor system. The blade

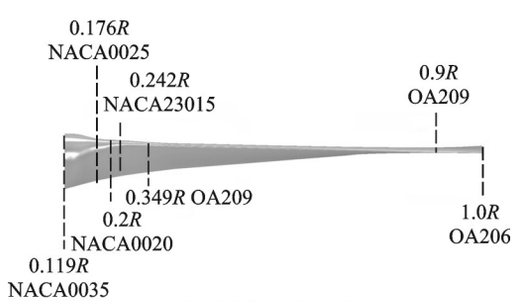

(a) Airfoil configuration

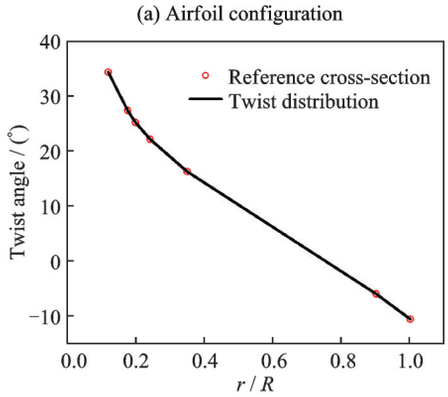

(b) Twist angle distribution

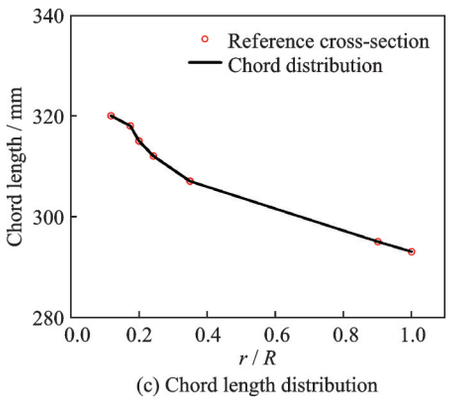

(c) Chord length distribution

Fig.2 Aerodynamic shape of rotor blades

root section primarily employs thick NACA symmetric airfoils, while the mid-span and tip sections adopt OA series airfoils. The chord length and negative twist exhibit nonlinear distributions along the span(r/R). Table 1 provides the geometric parameters of the rotors.

Table 1 Rotor parameters

Parameter	Value	Parameter	Value
Rotor diameter/m	3.2	Number of blades/(piece×set)	2×6
Root cut ratio	0.119	Rotational speed/(r•min^{-1})	1 300
Pitch angle ($0.75R$)/(°)	8	Installation configuration	Twin-blade rotor

Fig.3(a) shows the top view of the H6 overlapping configuration layout of the heavy-load eVTOL aircraft, and Fig.3(b) shows its side view. The axial spacing H between rotors is 0.5 m, and the longitudinal spacing x is 2.25 m.

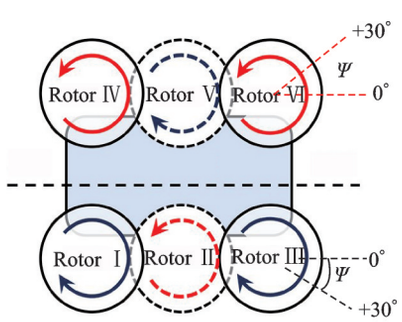

(a) Rotor layout and direction of rotation

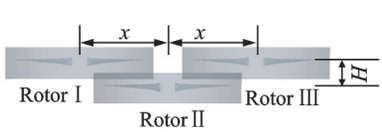

(b) Side view of rotor relative height

Fig.3 Layout characteristics of H6 overlapping configuration for heavy-load eVTOL aircraft

1.2 Numerical simulation method

This study employs the Reynolds-averaged Navier-Stokes (RANS) method to establish a numerical simulation approach for the aerodynamic characteristics of eVTOL aircraft. The Spalart-Allmaras (S-A) turbulence model is selected, and the N-S equations are solved to develop a numerical simulation method for rotor flow field and aerodynamic characteristics, shown as

$$\frac{\partial}{\partial t}\iiint_{\Omega} \boldsymbol{W}\mathrm{d}\Omega + \iint_{\partial\Omega}(\boldsymbol{F}_{\mathrm{c}} - \boldsymbol{F}_{\mathrm{v}})\mathrm{d}S = 0 \tag{1}$$

where $\boldsymbol{W}$ is the conservative variable, $\boldsymbol{F}_{\mathrm{c}}$ the convective flux term, and $\boldsymbol{F}_{\mathrm{v}}$ the viscous flux term. The specific expressions are as follows

$$\boldsymbol{W} = \begin{bmatrix} \rho \\ \rho u \\ \rho v \\ \rho w \\ \rho E \end{bmatrix}, \boldsymbol{F}_{\mathrm{c}} = \begin{bmatrix} \rho V_{\mathrm{r}} \\ \rho u V_{\mathrm{r}} + n_x p \\ \rho v V_{\mathrm{r}} + n_y p \\ \rho w V_{\mathrm{r}} + n_z p \\ \rho H V_{\mathrm{r}} + V_{\mathrm{t}} p \end{bmatrix}$$

$$\boldsymbol{F}_{\mathrm{v}} = \begin{bmatrix} 0 \\ n_x\tau_{xx} + n_y\tau_{xy} + n_z\tau_{xz} \\ n_x\tau_{yx} + n_y\tau_{yy} + n_z\tau_{yz} \\ n_x\tau_{zx} + n_y\tau_{zy} + n_z\tau_{zz} \\ n_x\Theta_x + n_y\Theta_y + n_z\Theta_z \end{bmatrix} \tag{2}$$

where ρ, E, H and p represent the air density, the total energy, the total enthalpy, and the pressure, respectively; V_{r} denotes the moving velocity of the control volume boundary (i.e., grid boundary), expressed as

$$\begin{cases} V_{\mathrm{r}} = V - V_{\mathrm{t}} = n_x u + n_y v + n_z w - V_{\mathrm{t}} \\ V_{\mathrm{t}} = n_x\dfrac{\partial x}{\partial t} + n_y\dfrac{\partial y}{\partial t} + n_z\dfrac{\partial z}{\partial t} \end{cases} \tag{3}$$

For spatial discretization, the Jameson second-order central difference scheme with artificial viscosity is used to discretize the conservative integral form of the flow field governing equations. The time advancement adopts the LU-SGS implicit scheme with the second-order accuracy. The environmental parameters are specified in Table 2.

Table 2 Environmental parameters

Aerodynamic viscosity/(Pa•s)	Air density/(kg•m^{-3})	Atmospheric pressure/Pa	Ambient temperature/°F
1.81E−5	1.205	99 700	288.15

1.3 Grid generation

A cuboid of $10L\times10L\times15L$ (where L is the fuselage length) is used as the flow field computational domain. Considering hover as a typical operating condition, in which the unsteady aerodynamic interference effects caused by complex rotor-rotor interactions are significantly higher than those in forward flight or other flight states, and to reduce the grid count, only half of the fuselage/rotor flow field is numerically simulated. The grid generation parameters are listed in Table 3, and the grid structures for the background domain and nested domains are shown in Fig.4. As the rotors undergo rotational motion, the sliding grid technique is employed. The grid is divided into moving and stationary grids. During numerical simulation, the moving grid rotates, and the flow field information is exchanged across the sliding interface between the moving and stationary grids. It is essential to ensure consistent grid density at the interface between the rotor region and the far-field/fuselage region to prevent multiple grid correspondences at the interface. Additionally, to better capture the boundary layer flow, prismatic boundary layer grids are generated on the fuselage and rotor surfaces, with a growth rate of 1.3 and 15 layers, satisfying $y^+<1$. The total grid nodes are 3.01 million, with 3.95 million boundary layer grid nodes.

Table 3 Grid parameters

Background domain grid		Nested domain grid	
Parameter	Value	Parameter	Value
Grid type	Cutting body grid	Grid type	Cutting body + Prism layer grid
Area size/(m×m×m)	18×30×30	Area size $H\times R$/(m×m)	1.5×2
Number of grids	6.51×10^6	Number of grids	6.48×10^6
Maximum grid size/m	0.8	Prism layer thickness/m	0.06
Surface grid size/m	0.8	Number of prism layers	15

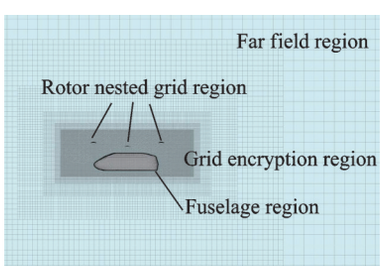

(a) Definition of flow field domain

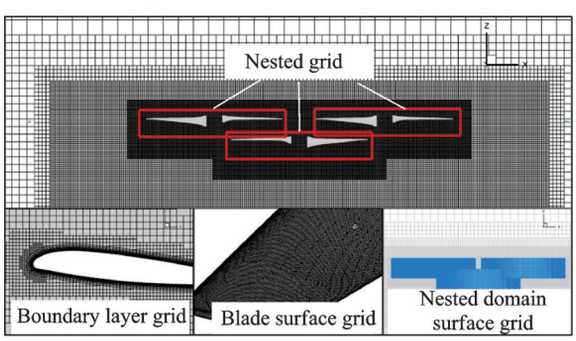

(b) Nested grid

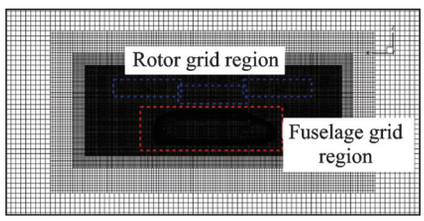

(c) Rotor/fuselage grid

Fig.4 Grid drawing method

1.4 Method validation

To validate the effectiveness of the numerical simulation method and grid generation results, isolated rotor aerodynamic performance tests were conducted at the National Key Laboratory of Helicopter Dynamics, Nanjing University of Aeronautics and Astronautics (Fig.5). Fig.6 compares the hovering thrust and the power of the isolated rotor obtained from numerical simulation and experimental data across different rotational speeds. The results show a good agreement between the numerical simulation and experimental data, confirming that the CFD method established in this study can accurately compute blade aerodynamic characteristics.

Grid independence verification is a necessary procedure to ensure the reliability of computational

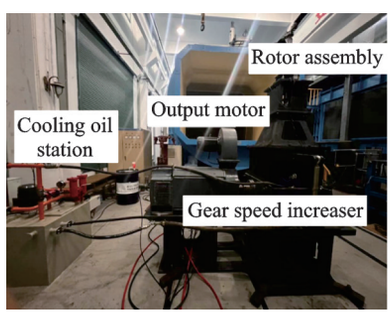

Fig.5 Rotor aerodynamic performance test bench

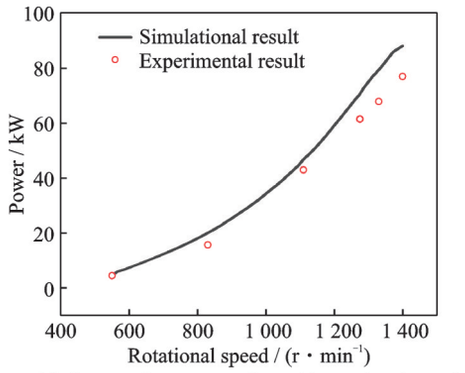

(a) Curves of power varying with rotational speed

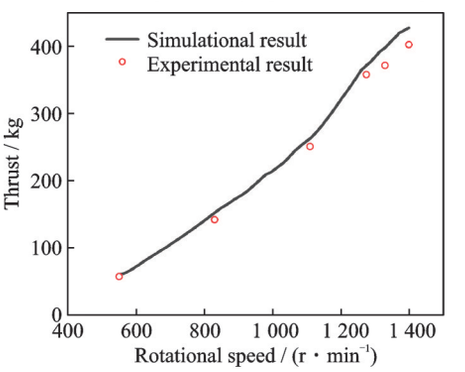

(b) Curves of thrust varying with rotational speed

Fig.6 Example verification

results. Generally, increasing grid resolution in the computational domain enhances the capture of turbulent vortex structures but conflicts with the significant increase in computational resource consumption and the reduced solution efficiency. Three grid sets (coarse, medium, and fine) with 9.61×10^6, 12.99×10^6, and 20.16×10^6 cells, respectively, were generated. The computational results are presented in Table 4, indicating that the medium grid achieves the required accuracy, striking an engineering balance between computational precision and efficiency.

Table 4 Comparison of grid independence verification

Grid	Number of grids/10^4	Thrust/kg	Power/kW
Coarse	961	372.45	75.98
Medium	1 299	360.14	72.32
Fine	2 016	355.86	69.18

2 Computational Result Analysis

This section conducts a computational analysis of the aerodynamic performance and inter-rotor aerodynamic interference characteristics of overlapping rotors in hover. By comparing the computational results of rotor aerodynamic performance, the normal force distribution across the rotor disk plane, and the blade-vortex interaction (BVI), the aerodynamic interference mechanism in the unsteady flow field of the overlapping rotor layout during hover is analyzed.

To more intuitively reflect the impact of aerodynamic interference on rotor aerodynamic performance, the thrust coefficient C_t, the thrust interference coefficient K, the power coefficient m_k, and the hover efficiency F_M are introduced, with their expressions shown as follows

$$C_t=\frac{T}{\frac{1}{2}\rho V^2 S} \tag{4}$$

$$K=T/T_{\mathrm{SINGLE}} \tag{5}$$

$$m_k=\frac{P}{\frac{1}{2}\rho V^3 S} \tag{6}$$

$$F_M=\frac{1}{2}\times\frac{C_L^{3/2}}{m_k} \tag{7}$$

where T is the thrust of a single rotor in the multi-rotor configuration, T_{SINGLE} the thrust of the isolated rotor, P the power, ρ the air density, C_L the lift coefficient, V the blade tip speed, and S the rotor disk area.

2.1 Aerodynamic performance

Fig.7 shows the variations in instantaneous thrust and power of Rotors Ⅰ, Ⅱ, and Ⅲ over one rotation cycle. The instantaneous thrust and power distribution curves exhibit obvious periodicity with a frequency of 2/rev. This is because each rotor group has two blades, and the blades encounter each other twice within one rotation cycle at azimuth angles of 0° and 180°, respectively. To analyze the thrust and power fluctuations of each rotor over one rotation cycle, Table 5 presents the statistical results of thrust and power data.

The black and blue curves in Fig.7 represent the variations in thrust and power of Rotors Ⅰ and Ⅲ with respect to the azimuth angle over one rotation cycle, respectively. Combining the statistical results in Table 5, it can be seen that the thrust and power trends of Rotors Ⅰ and Ⅲ are the same, and the fluctuation amplitudes are relatively small. When encountering Rotor Ⅱ (azimuth angles= 0°, 180°), affected by the inter-rotor aerodynamic interference, both the thrust and the power reach their

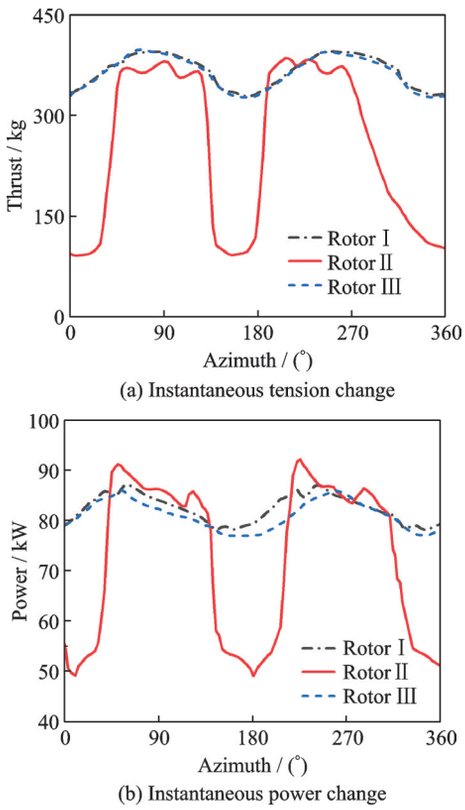

Fig.7 Instantaneous thrust and power changes within one rotation cycle

Table 5 Statistical results of tension and power data within one rotation cycle

Parameter	Rotor Ⅰ		Rotor Ⅱ		Rotor Ⅲ	
	Thrust/kg	Power/kW	Thrust/kg	Power/kW	Thrust/kg	Power/kW
Maximum	395.1	87.28	385.3	92.02	396.8	86.22
Minimum	326.8	77.73	89.46	48.12	325.9	76.74
Mean	365.4	82.25	262.7	73.76	363.6	81.16
Standard deviation	23.68	2.73	122.1	15.24	24.30	2.96

troughs. When the rotors are parallel to each other (azimuth angles=90°, 270°), the thrust and the required power reach their peaks. The thrust recovers to the normal level under isolated rotor conditions, while the required power still exceeds 72 kW. This indicates that the flow field characteristics near Rotors Ⅰ and Ⅲ are basically the same, and the influence of aerodynamic interference on them is relatively small, mainly causing an increase in the required power. The red curve in Fig.7 represents the variations in thrust and power of Rotor Ⅱ with respect to the azimuth angle over one rotation cycle. Combining the statistical results in Table 5, it can be seen that due to the influence of inter-rotor aerodynamic interference, the thrust and power of Rotor Ⅱ exhibit large fluctuations over one rotation cycle. When encountering Rotors Ⅰ and Ⅲ (azimuth angles=0°, 180°), severely affected by the inter-rotor aerodynamic interference, the thrust and the power of Rotor Ⅱ drop sharply to their lowest values, i.e. 90 kg and 48 kW, respectively. When parallel to Rotors Ⅰ and Ⅲ (azimuth angles = 90°, 270°), the influence of inter-rotor aerodynamic interference is the smallest. The rotor thrust recovers to 360 kg, while the required power reaches 91 kW, seriously exceeding the designed rated power. This indicates that due to the influence of inter-rotor aerodynamic interference, the thrust and the power of Rotor Ⅱ exhibit large fluctuations over one rotation cycle, and the unsteady flow field around the rotor is complex.

Table 6 presents the mean thrust L, the mean power Q, the power coefficient m_k, the thrust coefficient C_t, the thrust interference coefficient K, and the hover efficiency F_M of Rotors Ⅰ, Ⅱ, and Ⅲ over one rotation cycle, and compares them with the computational results of the isolated rotor. Compared with the isolated rotor, the thrust performance of Rotors Ⅰ and Ⅲ is basically the same as that under isolated rotor conditions, the required power increases by approximately 14.6%, and the hover efficiency decreases by 8.89%. The thrust of Rotor Ⅱ decreases by 26.4%, the required power increases by 3.37%, and the hover efficiency decreases by 38%, which once again proves that Rotor Ⅱ is severely affected by the aerodynamic interference.

Table 6 Comparison of aerodynamic performance

Parameter	Isolated rotor	Rotor Ⅰ	Rotor Ⅱ	Rotor Ⅲ
L/kg	360.14	365.37	262.66	363.62
C_t	0.604	0.622	0.447	0.619
K		1.014	0.739	1.009
Q/kW	72.32	82.25	73.76	81.16
m_k	0.361	0.412	0.370	0.407
F_M	0.652	0.594	0.404	0.598

2.2 Aerodynamic force distribution

Fig.8 shows the normal force contour plots of

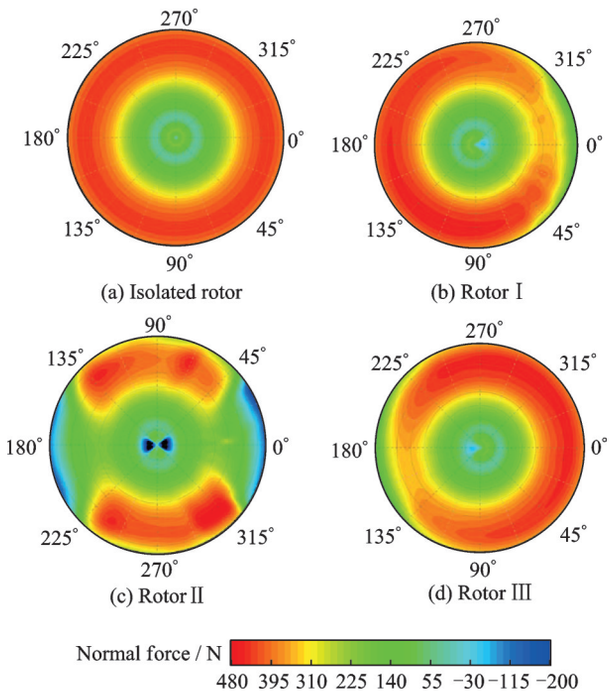

Fig.8 Cloud diagram of normal force on the plane of the rotor disc

the rotor disk planes for the isolated rotor, Rotor Ⅰ, Rotor Ⅱ, and Rotor Ⅲ. Firstly, under the influence of aerodynamic interference, the overlapping rotors experience varying degrees of normal force loss near the blade tips, and the normal force distribution at the blade tips shows obvious fluctuations. Secondly, the normal force distributions on the rotor disk planes of Rotors Ⅰ and Ⅲ follow the same pattern. That is, when the three rotors encounter each other (azimuth angle of Rotor Ⅰ = 0°, azimuth angle of Rotor Ⅲ = 180°), the normal force loss at the blade tips is the most severe. Within the range of 45° azimuth angles before and after the rotor encounter, the normal force near the blade tips changes significantly. Finally, the area of the low-load region at the center of Rotor Ⅱ's rotor disk expands. This is because Rotor Ⅱ is located in the downwash region of the other two rotors and is continuously affected by the wake flow. Within the range of 45° azimuth angles before and after the rotor encounter, the normal force loss in the mid-span and blade tip regions of the blades is severe, and even negative thrust phenomena occur near the blade tips. This is due to severe BVI in the blade tip region of Rotor Ⅱ.

2.3 Flow field pattern distribution

Fig.9 shows the variations in surface pressure distribution on the upper and lower surfaces of Rotors Ⅰ, Ⅱ, and Ⅲ over one rotation cycle. When Rotor Ⅰ encounters Rotor Ⅱ, due to the blade encounter interference effect, the flow velocity on the lower surface of Rotor Ⅰ increases, and the surface pressure decreases, resulting in a decrease in the thrust of Rotor Ⅰ. At the same time, the blade tip vortex shed from Rotor Ⅰ collides with Rotor Ⅱ, causing a local pressure surge on the upper surface of Rotor Ⅱ, which leads to a decrease in the thrust of Rotor Ⅱ near the azimuth angle of 180°. When Rotor Ⅲ encounters Rotor Ⅱ, due to the presence of turbulence in the flow field, the surface pressure on the lower surface of Rotor Ⅲ fluctuates significantly, and the negative pressure region on the upper surface shrinks. This further explains the reasons for the decrease in the thrust of Rotor Ⅲ near the azimuth angle of 180° in Fig.7 and the fluctuation of the normal force on the rotor disk of Rotor Ⅲ within the range of 150°—210° azimuth angles in Fig.8. Moreover, the influence of inter-rotor aerodynamic interference on Rotor Ⅲ is more significant.

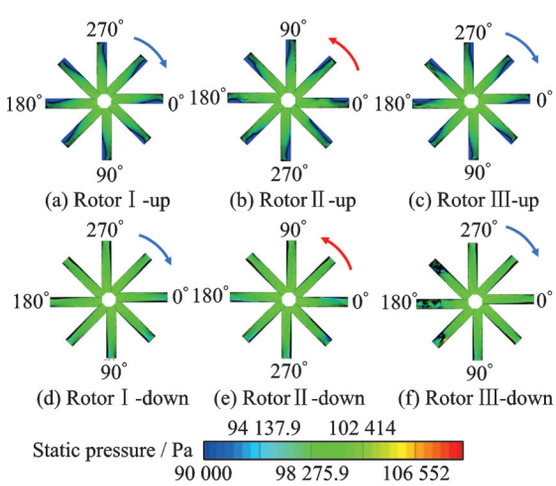

Fig.9 Pressure distribution on the upper and lower wing surfaces of each rolor

To further analyze the influence of aerodynamic interference on the hover flow field of overlapping Rotors Ⅰ, Ⅱ, and Ⅲ, Fig.10 intercepts the downwash velocity distributions of the longitudinal sections of the rotor disks of Rotors Ⅰ, Ⅱ, and Ⅲ ($x = -2.6, 0, 2.6$ m) and the middle positions of

the overlapping regions of the rotor disks (x = −1.3, 1.3 m), and also plots the streamline distributions within the sections. At this time, the azimuth angle of the rotors is 90°, and the three rotor groups are arranged in parallel.

Fig.10(b) shows the downwash velocity distribution within the rotor disk section of Rotor Ⅰ. It can be observed that the airflow above the rotor is accelerated by the downwash velocity of the rotor, and the airflow rapidly passes through the gap between Blade 1 and Blade 1′. Figs.10(d) and 10(f) show the downwash velocity distributions within the rotor disk sections of Rotors Ⅱ and Ⅲ, respectively. At this time, due to the presence of a turbulent region between x = 0 — 2.6 m, the flow velocity above the rotor disks of Rotors Ⅱ and Ⅲ is high, forming a negative pressure region. This causes the airflow below Blade 3 and Blade 5 to be re-attracted to the upper side of the blades, resulting in blade tip flow separation and a decrease in rotor thrust.

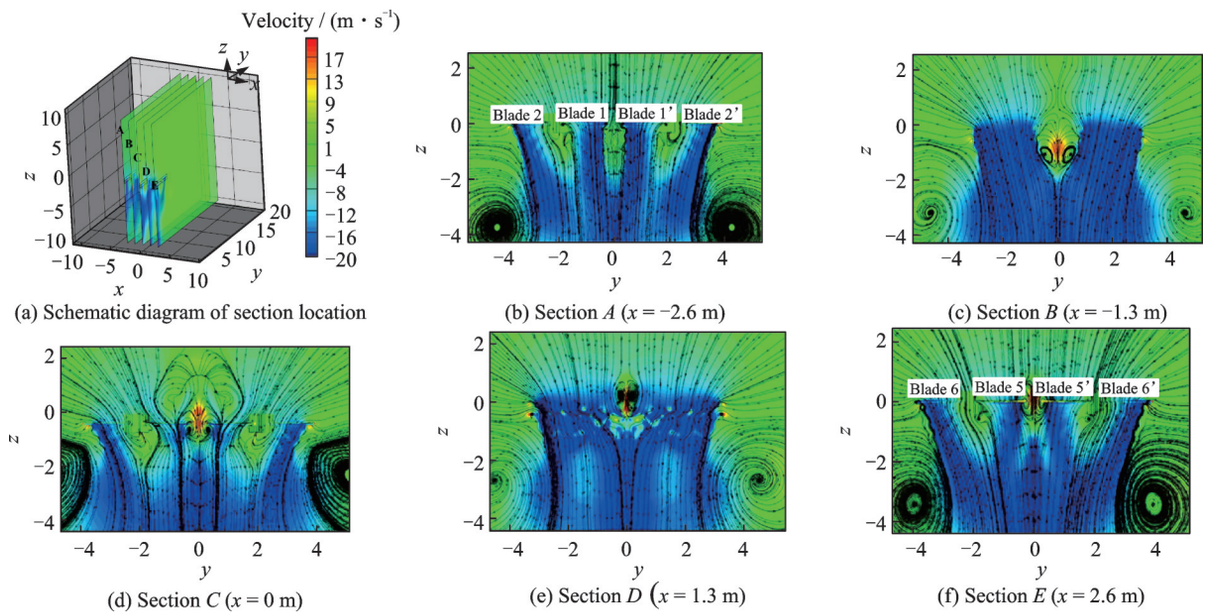

Fig.10 Distribution of downwash velocity on the rotor disc profile

3 Blade-Vortex Interaction Analysis

Blade-vortex interaction is the fundamental cause of the reduction in rotor aerodynamic performance. For overlapping rotors, the blade-vortex interaction phenomena mainly fall into the following two types: (1) Intra-rotor blade-vortex interaction, where the tip vortex shed from one blade of the same rotor pair strikes the surface of another blade, causing aerodynamic interference; (2) inter-rotor blade-vortex interaction, where the tip vortex shed from one rotor pair strikes the surface of another rotor pair, causing aerodynamic interference. According to Fig.7, during one rotation cycle, when Rotors Ⅰ, Ⅱ, and Ⅲ encounter each other, the inter-rotor aerodynamic interference phenomenon is the most pronounced. Therefore, this section mainly focuses on the analysis of the hovering flow field when the overlapping rotors meet.

3.1 Isolated rotor tip vortices

Fig.11 presents the vorticity distribution contour plots of the rotor disk cross-section and the tip vortex schematic diagram of an isolated single rotor under hovering conditions. Among them, Fig.11(a) is the vorticity distribution contour plot of the rotor disk cross-section, Fig.11(b) is the vorticity distribution contour plot of the rotor disk longitudinal cross-section, and Fig.11(c) visualizes the flow field using the Q-criterion vorticity isosurface and colors it with vorticity. The vorticity distribution of the isolated single rotor's disk cross-section has a centrally symmetric characteristic, with relatively low tip vortex intensity and a small range of action.

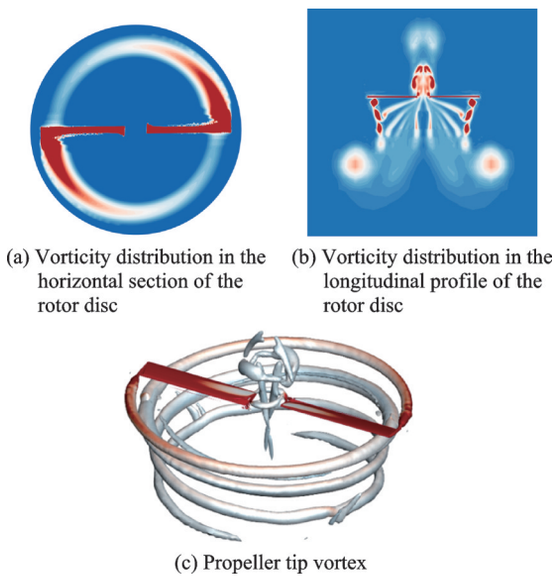

Fig.11 Vortex cloud map and tip vortex of isolated rotor

Meanwhile, due to the absence of aerodynamic interference, the tip vortex rapidly deviates from the rotor disk plane after shedding, effectively avoiding intra-rotor blade-vortex interaction.

3.2 Blade-vortex interactions between overlapping rotors

Fig.12 shows the evolution process (State 1—State 4) of the tip vortices of three rotor groups under hovering conditions. It can be observed that due to the influence of the downwash of Rotor Ⅱ, within the overlapping area of the rotor disks, the tip-shed vortex of Rotor Ⅰ moves downward after shedding from the rotor disk. Meanwhile, the diameter of the vortex filament becomes thinner and the vortex intensity decreases. In the independent area, the vortex filaments are regularly distributed and have relatively high intensity. In the overlapping area of Rotors Ⅱ and Ⅲ, for Rotor Ⅲ located above, its tip vortex moves downward after shedding from the blade trailing edge. Before reaching the rotor disk of Rotor Ⅱ, it is affected by the upwash of Rotor Ⅱ and is re-entrained back to the rotor disk plane of Rotor Ⅲ. At the same time, due to the high airflow velocity in the area near the tip of the symmetric-side rotor blades, there is a negative pressure area, which gives the tip vortex of Rotor Ⅲ a velocity component in the negative y-axis direction. It then interferes with the tip vortex shed from

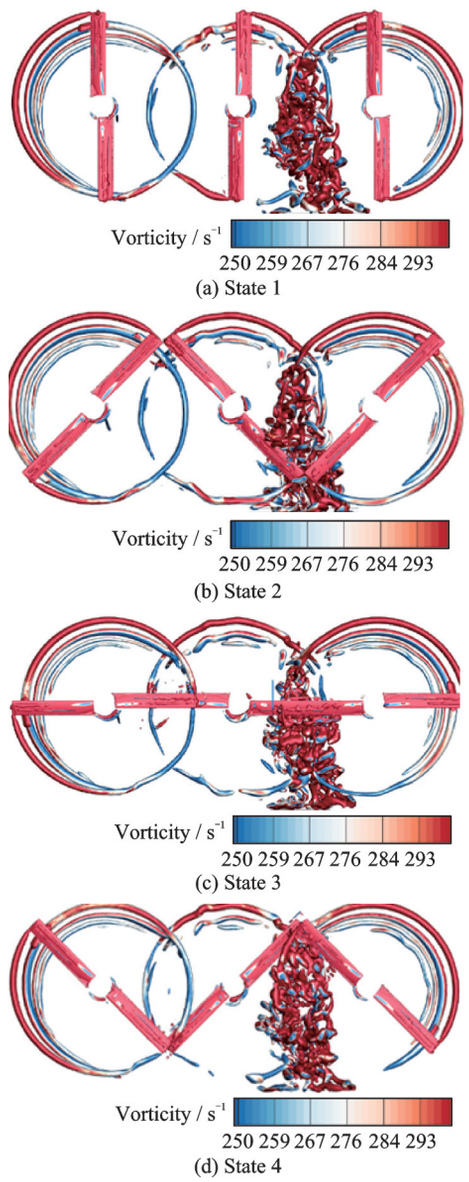

Fig.12 Evolution process of overlapping rotor tip vortices under hovering conditions

Rotor Ⅱ, ultimately forming the turbulent phenomenon shown in Fig.12, which explains the significant lift fluctuation of Rotor Ⅱ in the azimuth angle range of 135°—225° in Fig.7.

Fig.13 provides a partial enlarged view of the tip vortices of Rotors Ⅰ, Ⅱ, and Ⅲ at an azimuth angle of 45°. It can be observed that before reaching the rotor disk plane of Rotor Ⅱ, the tip vortices shed from each blade of Rotors Ⅰ and Ⅲ are regularly distributed. When they reach the rotor disk of Rotor Ⅱ, severe blade-vortex interaction occurs, and the vortex filaments show obvious deformation and fusion. As shown in Fig.13(a), at this time,

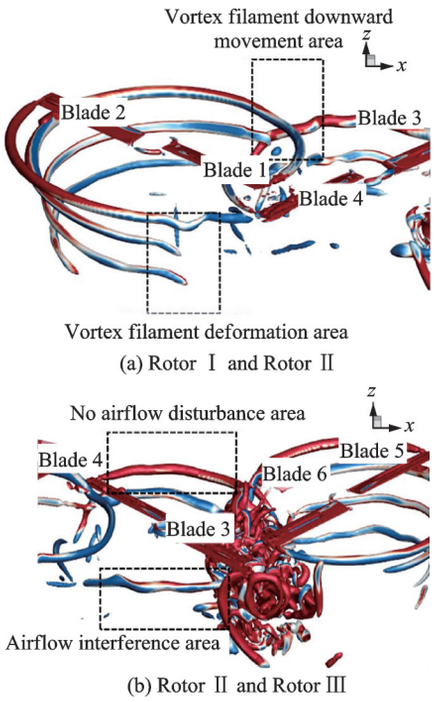

Fig.13 Aerodynamic interference flow field of rotor blades

Blade 1 and Blade 4 are moving away from each other. It can be clearly observed that the tip vortex shed from Blade 1 is rapidly separated from the rotor disk plane under the influence of the downwash of Blade 3. The diameter of the vortex filament becomes thinner and the vortex intensity decreases. At the same time, Blade 3 directly collides with the tip vortex shed from Blade 2, causing problems such as flow separation on the surface of Blade 3 and a reduction in blade lift. Moreover, the tip-shed vortex of Blade 3 also shows vortex filament deformation and twisting phenomena. Fig.13(b) shows the occurrence of turbulence in the overlapping area of Rotors Ⅱ and Ⅲ. At this time, Blade 3 and Blade 6 meet, and the shed vortices of the two blades are extremely irregularly distributed and tend to move in the negative y-axis direction. A comparative analysis of the tip vortices shed from Blade 3 and Blade 4 shows that Blade 3 is located at the intersection of the flow fields of Rotor Ⅰ, Rotor Ⅲ, and the symmetric-side rotor. Affected by the airflow disturbances from these three, the blade-vortex deformation is severe.

Fig.14 presents a partial enlarged view of the blade-vortex interaction at an azimuth angle of 0°. Fig.14(a) shows the vorticity isosurface distribution contour plot of the hovering interference flow field. It can be observed that the tip vortex shed from Blade 2 collides with Blade 4 after half a rotation cycle. Due to the influence of turbulence, Blade 3 shows obvious flow separation phenomena. Fig.14(b) shows the pressure distribution on the blade surfaces of Blades 3 and 4 under the influence of the shed vortices of the other rotors. It can be observed that the area of the negative pressure region on the upper surface of the middle section of Blade 4 shrinks, and there is a local sudden increase in surface pressure at the blade leading edge. The surface pressure on the upper surface of the trailing edge of Blade 3 increases. This proves that at this time, due to the influence of airflow disturbances, flow separation occurs at the trailing edge position of the upper surface of the blade, resulting in a reduction in blade lift, an increase in aerodynamic drag, and an increase in required power.

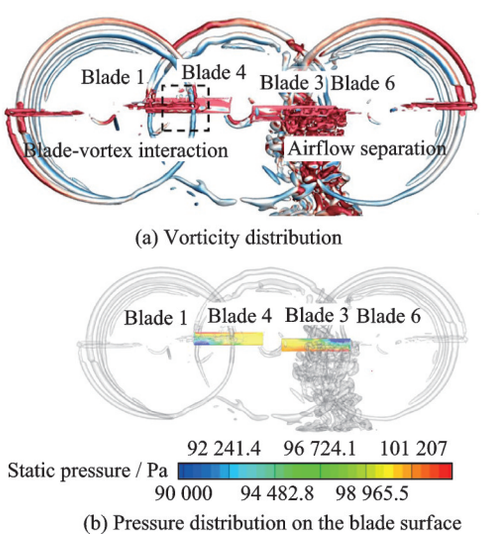

Fig.14 Local enlarged view of 14 blade vortex interference (azimuth=0°)

3.3 Analysis of the interference flow field between overlapping rotors and fuselage

3.3.1 Flow field streamline analysis

When the eVTOL is in a hovering state, the rotor downwash directly strikes the fuselage, generating additional downwash loads. At this time, the interference between the rotors and the fuselage is severe. Therefore, it is necessary to analyze the aerodynamic interference characteristics of the rotor/fuselage flow field during hovering. Fig.15 presents

the aerodynamic interference streamline diagram of the entire aircraft in a hovering state at the x-section ($x = 0$ m) passing through the rotation axis of Rotor Ⅱ. By analyzing the streamline distribution of the section, the interference characteristics between the rotors and the fuselage can be obtained. It can be seen that when the aircraft is in a hovering state, the rotor flow field is funnel-shaped. This is because the airflow above the rotors is attracted and accelerates downward. The airflow on the outer side of the rotors forms tip vortices due to the lack of obstruction from the fuselage. On the contrary, when the airflow on the inner side continues to move downward after passing through the rotors, part of the airflow encounters the obstruction of the fuselage and cannot move downward unobstructed. It is rolled up and flows upward. As the airflow continues to flow upward and is attracted by the rotors, a circulating flow is finally formed above the fuselage, similar to the "fountain effect" phenomenon of tiltrotor aircraft (Area A). Due to the limited width of the fuselage, most of the airflow is less obstructed by the fuselage and can smoothly pass through the fuselage (Area B).

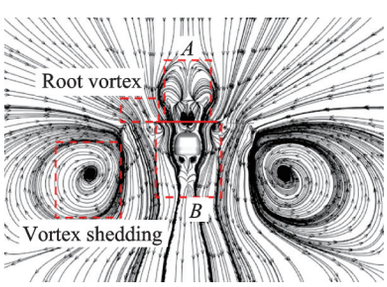

Fig.15 Central section streamline diagram of Rotor Ⅱ

Fig.16 shows the aerodynamic interference streamline diagram of the entire aircraft in a hovering state at the x-section ($x = 2.65$ m) passing through the rotation axis of Rotor Ⅰ and a partial enlarged view of the inner tip flow field. The center of the rotor disk of Rotor Ⅰ is located at the front of the fuselage, and there is no fuselage obstruction to the airflow below. Therefore, the rotor flow field is funnel-shaped, and the airflow on the outer side can smoothly pass through the rotor disk and move downward without obstruction. The figure shows the streamline distribution of the rotor disk cross-section when two lateral rotor groups meet. At this time, due to the small lateral spacing between the two rotor groups, the tip vortices shed from the inner two blades collide and fuse near the rotor disk. Due to the acceleration effect of the downwash, they rapidly move downward. The situation of Rotor Ⅲ is basically the same as that of Rotor Ⅰ and will not be repeated here.

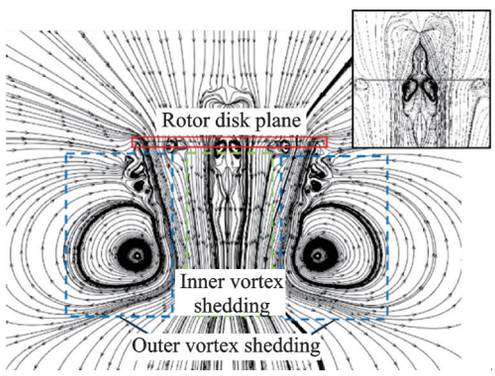

Fig.16 Central section streamline diagram and partial enlarged view of Rotor Ⅰ

3.3.2 Interference characteristic analysis

Complex aerodynamic interference phenomena exist in the hovering flow field of overlapping rotors. Figs.17(a,b) present the vorticity isosurface distribution contour plots of the hovering flow field of the half-fuselage model + overlapping rotor combined model. The wakes of the overlapping rotors exhibit both radial contraction and vertical convection movements. Among them, the tip vortices shed from the two rotor groups located above do not experience significant local disturbances before reaching the plane of the lower rotor, and the vortex filaments are relatively regularly distributed. As the tip vortices pass through the rotor disk of the lower rotor, they are disturbed by the tip vortices of the lower rotor, and the vortex filaments show obvious disturbances. Especially within the overlapping area of the rotor disks, the tip vortices of different rotors fluctuate violently, twist, deform, and merge. The wake of the lower rotor is always subject to the alternating interference of the shed vortices of the other two rotor groups, and the vortex filaments are chaotically distributed. Figs.17(c,d) are schematic diagrams of the pressure distribution on the fuselage surface. As the tip vortices of the three rotor groups continue to

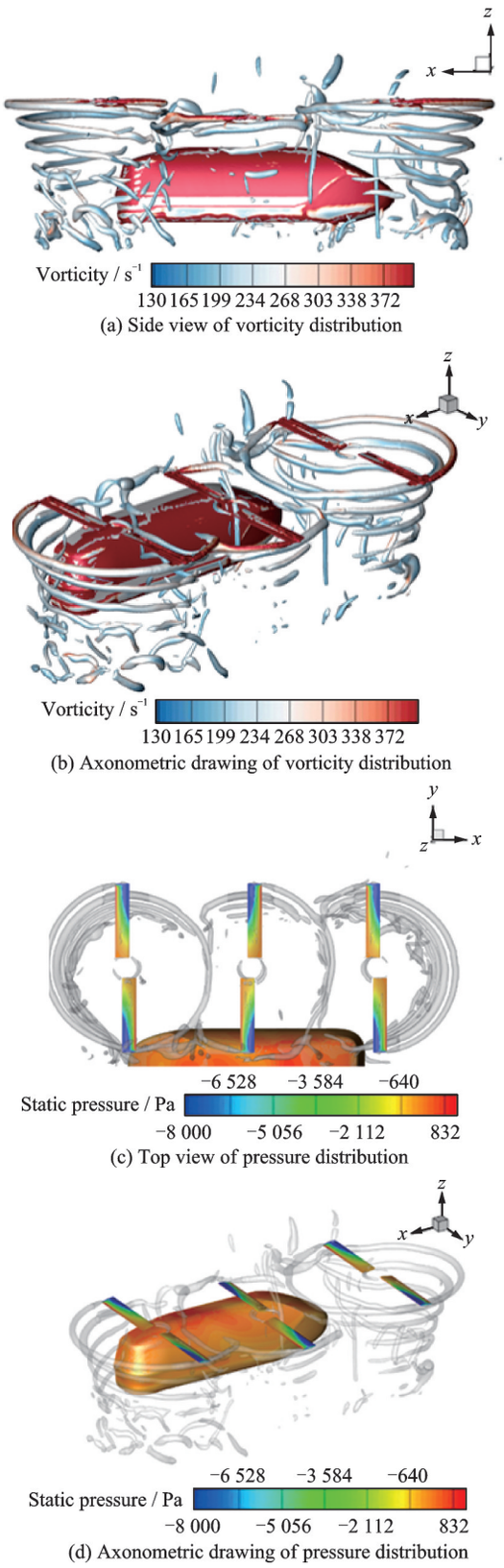

Fig.17 Overlapping rotor shedding vortex

move downward and reach the fuselage surface, the tip vortices collide with the fuselage, resulting in the dissipation of the tip vortices and a sudden increase in the pressure on the fuselage surface. Due to the small distance between the lower rotor and the top of the fuselage, the tip vortices shed from the lower rotor disk directly collide with the middle part of the fuselage, resulting in relatively high pressure on the fuselage surface.

4 Conclusions

This paper reveals the aerodynamic interference characteristics and evolution laws of the overlapping rotor configuration of heavy-load eVTOL aircraft in hover state through numerical simulation methods. The main conclusions are as follows.

(1) Periodic characteristics of rotor aerodynamic loads: The hover flow field analysis of the overlapping rotor system indicates that the instantaneous thrust and power parameters of the three sets of Rotors Ⅰ, Ⅱ, Ⅲ) exhibit significant periodic variations with the azimuth angle, with a dominant frequency of the second harmonic of the rotor rotational frequency (2/rev). This phenomenon originates from the phase coupling effect of aerodynamic interference between the rotors. Compared with the traditional coaxial rotor configuration, the overlapping layout significantly amplifies the amplitude of periodic fluctuations in rotor loads, providing a key theoretical basis for the design of vibration suppression and active control strategies.

(2) Blade-tip vortex interference mechanism and turbulence evolution: The complex vortex interactions between the rotors result in three typical interference modes. The blade-tip vortex shed from Rotor Ⅰ is impacted by the downwash flow of adjacent rotors, causing the vortex core structure to break at specific positions and triggering a significant attenuation of the axial component of the induced velocity field. Rotor Ⅱ, in the overlapping region, is continuously subjected to alternating vortex interference from the upper rotors, resulting in a non-uniform distribution of dynamic pressure across its rotor disk and a significant reduction in aerodynamic efficiency. After the blade-tip vortex of Rotor Ⅲ collides with the lower rotor, the vortex filaments undergo secondary rolling and form large-scale turbulent structures, with significantly en-

hanced turbulent fluctuation energy compared to the isolated rotor wake.

(3) Fuselage coupling effect and flow field distortion: The coupling effect between the semi-fuselage and the rotor system triggers two types of special flow field phenomena. The interaction between the downwash flow of Rotor Ⅱ and the fuselage boundary layer forms a self-sustaining circulating flow, generating a local high-pressure zone at the top of the fuselage and inducing a "fountain effect" similar to that of tiltrotor aircraft. When the blade-tip vortices of Rotors Ⅰ and Ⅲ penetrate the rotor disks of the lower rotors, the vortex core distortion occurs due to the influence of velocity gradients, and the asymmetric distribution of their induced velocity fields becomes the main cause of aerodynamic force fluctuations.

References

[1] DENG Jinghui. Technical status and development of electric vertical takeoff and landing aircraft[J]. Acta Aeronautica et Astronautica Sinica, 2024, 45(5): 529937. (in Chinese)

[2] SYAL M, LEISHMAN J G. Aerodynamic optimization study of a coaxial rotor in hovering flight[J]. Journal of the American Helicopter Society, 2012, 57(4): 1-15.

[3] HAYAMI K, SUGAWARA H, TANABE Y, et al. Numerical investigation of aerodynamic interference on coaxial rotor[C]//Proceedings of the AIAA Scitech 2020 Forum. [S.l.]:AIAA, 2020.

[4] QI Haotian, PU Tianmei, ZHU Weijun, et al. Influence mechanism of configuration parameters on the aerodynamic interaction of rigid coaxial rotor in hover [J]. Journal of Yangzhou University (Natural Science Edition), 2024, 27(5): 59-67. (in Chinese)

[5] LU Taoye, CHEN Renliang, JI Honglei, et al. Performance analysis of coaxial rotor for hovering in ground effect[J]. Journal of Harbin Institute of Technology, 2017, 49(10): 45-52. (in Chinese)

[6] ZHANG Tianyi, XU Guohua, SHI Yongjie, et al. Numerical simulation and analysis of helicopter rotor/ fuselage/horizontal tail interaction based on moving embedded grid[J]. Journal of Nanjing University of Aeronautics & Astronautic, 2024, 56(3): 534-544. (in Chinese)

[7] LEI Y, JI Y, WANG C. Optimization of aerodynamic performance for coaxial rotors with different rotor spacings[J]. International Journal of Micro Air Vehicles, 2018, 10(4): 362-369.

[8] LEI Y, BAI Y, XU Z J, et al. An experimental investigation on aerodynamic performance of a coaxial rotor system with different rotor spacing and wind speed[J]. Experimental Thermal and Fluid Science, 2013, 44: 779-785.

[9] WANG M S, CAO Y H. A review of coaxial compound helicopters: Aerodynamics and flight dynamics [J]. Archives of Computational Methods in Engineering, 2025, 32: 4001-4031.

[10] LIANG Jiahui, ZHANG Xiayang, ZHAO Qijun. Aerodynamic interference characteristics of a new compound configuration helicopter[J]. Journal of Beijing University of Aeronautics and Astronautics, 2025, 51 (3): 922-932. (in Chinese)

[11] ZHU Zheng, ZHAO Qijun, LI Peng. Unsteady flow interaction mechanism of coaxial rigid rotors in hover [J]. Acta Aeronautica et Astronautica Sinica, 2016, 37 (2): 568-578. (in Chinese)

[12] CUI Zhuangzhuang, YUAN Xin, ZHAO Qijun, et al. Computation for vertical flight performance of high speed helicopter based on CFD method[J]. Aerodynamic Research & Experiment, 2024, 2(5): 40-51.

[13] RAMASAMY M. Hover performance measurements toward understanding aerodynamic interference in coaxial, tandem, and tilt rotors[J]. Journal of the American Helicopter Society, 2015, 60(3): 1-17.

[14] TAN J F, CAI J G, BARAKOS G N, et al. Computational study on the aerodynamic interference between tandem rotors and nearby obstacles[J]. Journal of Aircraft, 2020, 57(3): 456-468.

[15] LI Zhuoyuan, YANG Xudong, SUN Kai, et al. Aerodynamic configuration of distributed ducted fan with complex strong interference effect and performance influence[J]. Acta Aeronautica et Astronautica Sinica, 2025, 46(3): 130805. (in Chinese)

[16] WANG Xuquan, JIANG Lusheng, SUN Huixun, et al. Computational investigation of the dual-thrust compound high-speed helicopter aerodynamic interactions in hover[J]. Helicopter Technology, 2024(4): 15-21. (in Chinese)

[17] LIU Yuan, CHEN Zhe, WANG Bo, et al. Analysis of aerodynamic interference and parameter influence on tilting multi rotor aircraft in forward flight state[J]. Flight Dynamics, 2024, 42(3): 40-44, 88. (in Chinese)

[18] LI Shangbin, JIANG Lusheng, LIN Yongfeng. The analysis of aerodynamic interference of tilt rotor aircraft in hover[J]. Engineering Mechanics, 2024, 41

(3): 232-240. (in Chinese)

Ackonwledgement This work was supported by the National Natural Science Foundation of China(No.11872211).

Author

The first/corresponding author Dr. **DU Siliang** obtained his Ph.D. from Nanjing University of Aeronautics and Astronautics in 2017 and is currently an associate professor at Huai'an University. He primarily engages in research and development work in the fields of aerodynamics, structure, and control of electric vertical take-off and landing (eVTOL) aircraft.

Author contributions Dr. **DU Siliang** designed the study, compiled the models, conducted the analysis. interpreted the results, and wrote the manuscript. Mr. **DENG Kai** revised the manuscript and contributed to the numerical simulation. Dr. **WANG Bo** contributed to the discussion and background of the study. All authors commented on the manuscript draft and approved the submission.

Competing interests The authors declare no competing interests.

(Production Editor: SUN Jing)

重载eVTOL飞行器重叠旋翼气动干扰特性数值模拟研究

杜思亮[1,2], 邓 凯[2], 王 博[2]

(1.淮安大学机械与材料工程学院, 淮安 223003,中国;
2.南京航空航天大学直升机动力学全国重点实验室, 南京 210016,中国)

摘要:针对重载电动垂直起降(Electric vertical takeoff and landing, eVTOL)飞行器重叠旋翼气动干扰机理不明的问题,本文通过数值模拟方法研究了重叠旋翼布局在悬停状态下的气动干扰特性及其流场演化规律。基于Reynolds-averaged Navier-Stokes (RANS)方程与Spalart-Allmaras (S-A)湍流模型,构建了旋翼流场及气动特性计算模型。结合运动嵌套网格技术实现了旋翼旋转运动的动态模拟,并通过网格无关性验证与试验数据对比确保了计算方法的可靠性。研究结果表明:重叠旋翼系统中,旋翼Ⅱ因持续受到相邻旋翼尾流及桨-涡干扰影响,拉力下降,功率波动显著,悬停效率降低;桨尖涡在重叠区域发生断裂、融合及二次卷起,形成大尺度湍流结构,导致诱导速度场衰减与气动效率损失;旋翼下洗流与机身干扰引发"喷泉效应"及机身表面压力突增,加剧了流场畸变。基于上述机理,通过优化相邻桨叶转速相位差的配置策略,可实现重叠旋翼构型的安全飞行,为重载eVTOL飞行器的旋翼布局设计与气动性能提升提供了理论依据。

关键词:电动垂直起降飞行器;重叠旋翼;气动干扰;数值模拟;桨-涡干扰

研究亮点:

1.通过数值模拟方法揭示了重载eVTOL飞行器重叠旋翼在悬停状态下的气动干扰特性及流场演化规律。

2.发现了桨尖涡在重叠区域的断裂、融合及二次卷起现象,以及由此导致的气动效率损失。

3.提出了通过优化相邻桨叶转速相位差配置策略来实现重叠旋翼构型安全飞行的解决方案。